
SIMULTANEOUS INFERENCE IN MULTIPLE MATRIX-VARIATE GRAPHS FOR HIGH-DIMENSIONAL NEURAL RECORDINGS

A PREPRINT

Zongge Liu *

Department of Statistics & Data Science
Carnegie Mellon University
Pittsburgh, PA 15213
zonggel@andrew.cmu.edu

Heejong Bong *

Department of Statistics
University of Michigan
Ann Arbor, MI 48109
hbong@umich.edu

Zhao Ren

Department of Statistics
University of Pittsburgh
Pittsburgh, PA 15260
zren@pitt.edu

Matthew A. Smith

Department of Biomedical Engineering
Carnegie Mellon University
Pittsburgh, PA 15213
msmith@andrew.cmu.edu

Robert E. Kass

Department of Statistics & Data Science
Carnegie Mellon University
Pittsburgh, PA 15213
kass@stat.cmu.edu

October 22, 2024

ABSTRACT

As large-scale neural recordings become common, many neuroscientific investigations are focused on identifying functional connectivity from spatio-temporal measurements in two or more brain areas across multiple sessions. Spatial-temporal data in neural recordings can be represented as matrix-variate data, with time as the first dimension and space as the second. In this paper, we exploit the multiple matrix-variate Gaussian Graphical model to encode the common underlying spatial functional connectivity across multiple sessions of neural recordings. By effectively integrating information across multiple graphs, we develop a novel inferential framework that allows simultaneous testing to detect meaningful connectivity for a target edge subset of arbitrary size. Our test statistics are based on a group penalized regression approach and a high-dimensional Gaussian approximation technique. The validity of simultaneous testing is demonstrated theoretically under mild assumptions on sample size and non-stationary autoregressive temporal dependence. Our test is nearly optimal in achieving the testable region boundary. Additionally, our method involves only convex optimization and parametric bootstrap, making it computationally attractive. We demonstrate the efficacy of the new method through both simulations and an experimental study involving multiple local field potential (LFP) recordings in the Prefrontal Cortex (PFC) and visual area V4 during a memory-guided saccade task.

Keywords Gaussian graphical model · Simultaneous testing · Multiple graphs · Heterogeneous learning · Bandable matrix

*The authors contribute equally to this paper.

1 Introduction

We address the problem of discovering associations between simultaneously recorded spatiotemporal datasets. A motivating example is neural recordings captured by two Utah arrays in a monkey’s brain. Each Utah array comprises a 10×10 square grid of electrodes on a $4.2\text{mm} \times 4.2\text{mm}$ base (Jones et al., 1992), and each electrode records pooled electrical signals or *local field potentials* from nearby neurons (Buzsáki et al., 2012). Khanna et al. (2020) recorded neural activity in both the visual (V4) and prefrontal (PFC) cortices during a spatial working memory task, producing 100 time series from each brain region. The coordinated activity between these two sets of time series can reveal the relationship between the two spatially-distant regions, or the *functional connection*.

When each dataset consists of a single time series, the coordinated activity between two datasets can be quantified using cross-correlation, calculated based on the replication structure within the datasets (Gubner, 2006). In neural experiments, each replication is referred to as an experimental trial, and a group of trials forms a session. While estimation precision increases with more trials, the duration of a single session is often constrained by physical, economic, and ethical factors. These limitations require pooling observations across multiple sessions, but the primary statistical challenge is accounting for the heterogeneity between trials from different sessions. Another challenge is the summarization of cross-correlations between all possible pairs of time series in the two spatiotemporal datasets. For instance, in a dataset with 100 time series from each brain region, there are 10,000 cross-regional pairs. To address this, we propose a novel statistical inference approach for the V4-PFC connection by assessing the global significance of these cross-regional interactions. We achieve this by employing a multiple matrix-variate Gaussian graphical model, where the spatial and temporal partial correlation parameters represent the association structure within the spatiotemporal datasets for each session.

Building on the matrix-variate Gaussian graphical model outlined above, we propose a three-step procedure for estimating and inferring the spatial partial correlations. First, we estimate the spatial partial correlation parameters across multiple sessions using a node-wise regression approach (Ren et al., 2019). Next, we estimate the temporal covariance parameters, assuming a mild bandable structure on their Cholesky factors, which will be used as nuisance parameters in the final inference step. Finally, leveraging the results from the first two steps, we construct a novel test statistic to evaluate the significance of individual edges or groups of edges. This inference framework draws inspiration from the linear functional-based tests of Ren et al. (2019), the debiased inference techniques for matrix-variate graphs from Chen and Liu (2018), and the high-dimensional Gaussian approximation methods by Chernozhukov et al. (2023b).

In addition, our work provides several methodological advancements and theoretical contributions. First, we develop a method for leveraging multiple session data collectively based on group lasso, enabling the discovery of a common spatial correlation graph across sessions with improved sensitivity. We demonstrate the improved inferential performance in theoretical analyses (Section 4) and simulation studies (Section 5). Second, while group lasso is a well-known method, its application and consistency in the context of auto-correlated samples have not been studied theoretically. In Section 4, we present a self-contained analysis, deriving rates of convergence for both estimation and prediction. This contribution may have broader implications for high-dimensional statistics involving correlated data. Finally, we provide theoretical guarantees for our proposed inference procedures, employing a Gaussian approximation bootstrap method based on Chernozhukov et al. (2023b). Notably, this is the first formulation of a global significance test for a group of edges in partial-correlation graphs, distinguishing our approach from existing FDR control methods.

1.1 Notations

For a vector \mathbf{x} , let $\|\mathbf{x}\|_p$ denote the ℓ_p -norm. For a real matrix X , we use $X_{i,\cdot}$ to denote the i -th row of X and $X_{\cdot,j}$ to denote the j -th column of X . Let $\|X\|_p$ denote the matrix p -norm, where $\|X\|_2$ is also referred to as the spectral or operator norm. We denote the Frobenius norm of X by $\|X\|_F$ and the entry-wise supremum norm by $\|X\|_\infty$. For any set A , its cardinality is denoted by $|A|$.

2 Matrix-variate Gaussian Graphical Model

Let $X \in \mathbb{R}^{p \times q}$ be the observed spatiotemporal data in a single trial. At a given time point t , $X_{t,\cdot} \in \mathbb{R}^q$ is vector-valued, with each entry of the vector corresponding to a specific spatial point. Vector-valued graphical models have been extensively employed to explore conditional dependence relationships in high-dimensional data, including neural recordings (Fornito et al., 2013; Vinci et al., 2018). In these models, each node in an undirected graph represents a vector entry, and two nodes are connected by an edge if and only if their corresponding entries exhibit conditional dependence given all other entries. When the random vector follows a multivariate Gaussian distribution, the partial correlations, or equivalently elements of the precision matrix, encode conditional dependencies between entries (Meinshausen and Bühlmann, 2006). Consequently, this type of graph is also referred to as a *partial-correlation graph*.

Since spatiotemporal data involve both time ($t = 1, \dots, p$) and space ($i = 1, \dots, q$), we consider a matrix-variate extension. A *matrix-variate Gaussian graphical model* (Dawid, 1981) is characterized by two covariance parameters: temporal (row) covariance matrix $\Sigma^{(\mathcal{T})} \in \mathbb{R}^{p \times p}$ and spatial (column) covariance matrix $\Sigma^{(\mathcal{S})} \in \mathbb{R}^{q \times q}$. The observed data X are said to follow the model with mean μ , denoted by $\text{MN}(\mu, \Sigma^{(\mathcal{T})}, \Sigma^{(\mathcal{S})})$, if and only if the vectorized matrix $\text{vec}(X)$ is vector-variate Gaussian distributed with mean $\text{vec}(\mu)$ and variance-covariance matrix $\Sigma^{(\mathcal{S})} \otimes \Sigma^{(\mathcal{T})}$, where \otimes denotes the Kronecker product. Due to the identifiability issue, hereafter we always assume that $\text{tr}(\Sigma^{(\mathcal{T})}) = p$ on the temporal (row) covariance. By imposing this Kronecker product structure, we reduce the number of parameters on the covariance from the order of p^2q^2 to $p^2 + q^2$, while achieving an interpretable covariance structure for both time and space. Indeed, this structure implies that the covariance between X_{ti} and X_{sj} is $\Sigma_{ts}^{(\mathcal{T})} \cdot \Sigma_{ij}^{(\mathcal{S})}$. If we denote the temporal (row) and spatial (column) precision matrices by $\Omega^{(\mathcal{T})} = (\Sigma^{(\mathcal{T})})^{-1}$ and $\Omega^{(\mathcal{S})} = (\Sigma^{(\mathcal{S})})^{-1}$, respectively, the inverse of $\Sigma^{(\mathcal{S})} \otimes \Sigma^{(\mathcal{T})}$ has a simple analytic form $(\Sigma^{(\mathcal{S})} \otimes \Sigma^{(\mathcal{T})})^{-1} = \Omega^{(\mathcal{S})} \otimes \Omega^{(\mathcal{T})}$. Due to the relationship between partial correlation and precision matrix, the partial correlation between space points i and j is given by $\rho_{ij}^{(\mathcal{S})} = -\Omega_{ij}^{(\mathcal{S})} / \sqrt{\Omega_{ii}^{(\mathcal{S})} \Omega_{jj}^{(\mathcal{S})}}$, invariant across time points (see Section 3.1).

3 Simultaneous Inference Framework

In this section we develop an inference framework for identifying spatial partial-correlation graphs in multiple spatiotemporal observations. The full procedure is summarized in Algorithm 1.

For each session $l = 1, \dots, m$, we observe spatiotemporal measurements in $p \times q$ matrix-variate sample over k trials. We assume each sample $X^{(k,l)}$ at trial k and session l follows matrix-variate Gaussian distribution $\text{MN}(0, \Sigma^{(\mathcal{T},l)}, \Sigma^{(\mathcal{S},l)})$, where $\Sigma^{(\mathcal{T},l)} \in \mathbb{R}^{p \times p}$ and $\Sigma^{(\mathcal{S},l)} \in \mathbb{R}^{q \times q}$ are the session-specific temporal and spatial covariance matrices, respectively. We denote the temporal and spatial precision matrices by $\Omega^{(\mathcal{T},l)} := (\Sigma^{(\mathcal{T},l)})^{-1}$ and $\Omega^{(\mathcal{S},l)} := (\Sigma^{(\mathcal{S},l)})^{-1}$, respectively.

Algorithm 1 Simultaneous Testing for Multiple Matrix-variate Gaussian Graphical Models

- 1: **Input:** Multi-session data \mathcal{D} , edge set \mathcal{S} , test level α
 - 2: **Output:** Confidence region $\mathcal{C}_E(1 - \alpha)$
 - 3: **Spatial precision matrix estimation:**
 - 4: **for** $i = 1 : q$ **do**
 - 5: Estimate the regression coefficient $\beta_{\cdot,i}^{(\mathcal{S},l)}$ and the residual $\epsilon_{\cdot,i}^{(\mathcal{S},k,l)}$ using Eq. (2).
 - 6: **end for**
 - 7: **for** $l = 1 : m, i = 1 : q, j = 1 : q$ **do**
 - 8: Estimate the de-biased residual variance $\Phi_{ij}^{(\mathcal{S},l)}$ using Eq. (3).
 - 9: Estimate the spatial precision $\Omega_{ij}^{(\mathcal{S},l)}$ and partial correlation $\rho_{ij}^{(\mathcal{S},l)}$ using Eq. (4).
 - 10: **end for**
 - 11: **Temporal precision matrix estimation:**
 - 12: **for** $l = 1 : m$ **do**
 - 13: Estimate the temporal regression coefficient $\beta^{(\mathcal{T},l)}$, residual variance $\Phi^{(\mathcal{T},l)}$ and temporal covariance $\Sigma^{(\mathcal{T},l)}$ using Eqs. (10), (11) and (13).
 - 14: **end for**
 - 15: **Hypothesis testing based on bootstrap:**
 - 16: Estimate the covariance matrix S_{EE} of the test statistic T_E using the plug-in estimator \widehat{S}_{EE} in Eq. (7).
 - 17: Sample $\{\widehat{Z}_i\}_{i=1,\dots,B} \sim N(0, \widehat{S}_{EE})$ and calculate the confidence region in Eq. (8).
 - 18: **return** Confidence region $\mathcal{C}_E(1 - \alpha)$
-

3.1 Estimation of Spatial Covariance Matrix

We begin by considering a single session l and time point t to motivate our node-wise regression approach (Meinshausen and Bühlmann, 2006; Liu, 2013). For the random variable $X_{ti}^{(k,l)}$, which represents electrode i at time t , its conditional distribution given the remaining variables in $X_{t,\cdot}^{(k,l)}$ follows a normal distribution and can be modeled as a linear regression:

$$X_{ti}^{(k,l)} = X_{t,\cdot}^{(k,l)} \beta_{\cdot,i}^{(S,l)} + \epsilon_{ti}^{(S,k,l)}, \quad (1)$$

where the regression coefficients are related to the spatial precision matrix via $\beta_{ji}^{(S,l)} = -\frac{\Omega_{ji}^{(S,l)}}{\Omega_{ii}^{(S,l)}} \mathbb{I}(i \neq j)$, and $\mathbb{E}[\epsilon_{ti}^{(S,k,l)}] = 0$. Due to the Kronecker product structure in the model, the regression coefficients are time-independent. Consequently, sparsity in the spatial precision matrix $\Omega^{(S,l)}$ implies corresponding sparsity in the regression coefficients $\beta^{(S,l)}$. A similar relationship holds between the spatial precision matrix and the covariance of the node-wise regression residuals. Specifically, for the residuals $\epsilon_{t,\cdot}^{(S,k,l)} = (\epsilon_{t1}^{(S,k,l)}, \dots, \epsilon_{tq}^{(S,k,l)})^\top$, the covariance is given by $\text{Cov}[\epsilon_{t,\cdot}^{(S,k,l)}] = \Sigma_{tt}^{(T,l)} \cdot \Phi^{(S,l)}$, where $\Phi^{(S,l)}$ is a time-independent matrix with elements defined as $\Phi_{ij}^{(S,l)} = \frac{\Omega_{ij}^{(S,l)}}{\Omega_{ii}^{(S,l)} \Omega_{jj}^{(S,l)}}$. Our target,

the spatial partial correlation, is expressed as $\rho_{ij}^{(S,l)} = -\frac{\Omega_{ij}^{(S,l)}}{\sqrt{\Omega_{ii}^{(S,l)} \Omega_{jj}^{(S,l)}}} = -\frac{\Phi_{ij}^{(S,l)}}{\sqrt{\Phi_{ii}^{(S,l)} \Phi_{jj}^{(S,l)}}}$, and testing $\Phi_{ij}^{(S,l)} = 0$ is equivalent to testing whether the partial correlation between i and j is zero. In Eq. (1), we treat each row of $X^{(k,l)}$ as a q -dimensional sample, giving us p correlated vector-valued samples for a sparse linear regression model, where the covariance among these ‘‘row samples’’ is characterized by $\Sigma^{(T,l)}$. Collecting all trials $k = 1, \dots, n_l$, we estimate $\Phi^{(S,l)}$ using $\hat{\Phi}^{(S,l)} = \mathbb{E} \left[\frac{1}{n_l p} \sum_{k=1}^{n_l} \sum_{t=1}^p \epsilon_{t,\cdot}^{(S,k,l)} \epsilon_{t,\cdot}^{(S,k,l)\top} \right]$, under the identifiability constraint $\text{tr}(\Sigma^{(T,l)}) = p$, where we effectively use $n_l p$ correlated samples in total.

Having discussed the model for individual sessions, we now consider all m sessions jointly to improve the estimation accuracy of each $\rho_{ij}^{(S,l)}$. Under assumption that the spatial precision matrices $\Omega_{ij}^{(S,l)}$ share the same sparsity pattern across sessions, the corresponding regression coefficients $\beta_{\cdot,i}^{(S,l)}$ also exhibit a common support across the m sessions. To harness this group sparsity assumption, we treat the coefficients $\beta_{ij}^{(S,1)}, \dots, \beta_{ij}^{(S,m)}$ as a group of parameters for each pair (i, j) and apply group lasso (Yuan and Lin, 2006) to the stacked m linear models, thereby improving estimation by borrowing strength across sessions:

$$\begin{aligned} & \{\hat{\beta}_{\cdot,i}^{(S,l)}\}_{l=1,\dots,m} := \\ & \underset{\{b^{(l)}\}_{l=1,\dots,m}}{\text{argmin}} \left\{ \frac{1}{2n_0 p} \sum_{l=1}^m \sum_{k=1}^{n_l} \|X_{\cdot,i}^{(k,l)} - X^{(k,l)} b^{(l)}\|_2^2 + \gamma_i \sum_{j:j \neq i} \sqrt{\sum_{l=1}^m \frac{\|\sum_k X_{\cdot,j}^{(k,l)}\|_2^2}{n_l p} b_j^{(l)2}} \right\}, \quad (2) \end{aligned}$$

with respect to $b_i^{(l)} = 0$ for all l , where $n_0 = \min_{1 \leq l \leq m} n_l$. The parameter γ_i can be tuned using cross-validation or other model selection methods.

Once the regression coefficients are estimated, the fitted residuals are computed as $\hat{\epsilon}_{ti}^{(S,k,l)} = X_{ti}^{(k,l)} - X_{t,\cdot}^{(k,l)} \hat{\beta}_{\cdot,i}^{(S,l)}$. Although the empirical covariance matrix of the fitted residuals provides a straightforward estimate of $\Phi_{ij}^{(S,l)}$, this estimate is biased due to the lasso-type penalty, leading to a larger error rate than the expected $1/\sqrt{n_l p}$ rate (Liu, 2013). To address this bias, we introduce a bias-correction term in the covariance estimate:

$$\hat{\Phi}_{ij}^{(S,l)} := \begin{cases} -\frac{1}{n_l p} \sum_{k=1}^{n_l} \sum_{t=1}^p \left(\hat{\epsilon}_{ti}^{(S,k,l)} \hat{\epsilon}_{tj}^{(S,k,l)} + \hat{\epsilon}_{tj}^{(S,k,l)2} \hat{\beta}_{ji}^{(S,l)} + \hat{\epsilon}_{ti}^{(S,k,l)2} \hat{\beta}_{ij}^{(S,l)} \right), & \text{if } i \neq j, \\ \frac{1}{n_l p} \sum_{k=1}^{n_l} \sum_{t=1}^p \hat{\epsilon}_{ti}^{(S,k,l)} \hat{\epsilon}_{tj}^{(S,k,l)}, & \text{if } i = j. \end{cases} \quad (3)$$

Using this bias-corrected estimate, we then estimate the spatial precision matrix $\Omega^{(S,l)}$ and the partial correlation matrix $\rho^{(S,l)}$ as follows:

$$\hat{\Omega}_{ij}^{(S,l)} := \frac{\hat{\Phi}_{ij}^{(S,l)}}{\hat{\Phi}_{ii}^{(S,l)} \hat{\Phi}_{jj}^{(S,l)}} \quad \text{and} \quad \hat{\rho}_{ij}^{(S,l)} := -\frac{\hat{\Phi}_{ij}^{(S,l)}}{\sqrt{\hat{\Phi}_{ii}^{(S,l)} \hat{\Phi}_{jj}^{(S,l)}}}. \quad (4)$$

While our partial correlation estimator is similar to the form proposed by Chen and Liu (2018) for a single matrix-variate Gaussian graphical model, our approach leverages information from multiple sessions using the group lasso estimate, leading to a faster convergence rate, as demonstrated in Theorem 4.1.

3.2 Simultaneous Test by Parametric Bootstrap

3.2.1 Single Edge Test

By leveraging information across m sessions using group lasso (Eq. (2)), we not only improve the efficiency of spatial partial correlation estimates but also enhance the power of tests for detecting significant associations. We first consider testing a single edge: for a pair (i, j) , the null hypothesis is

$$H_{0,ij} : \rho_{ij}^{(S,l)} = 0, \quad \forall l = 1, \dots, m. \quad (5)$$

Given the group sparsity structure, we construct a test statistic by aggregating the partial correlation estimates $\hat{\rho}_{ij}^{(S,l)}$ across all sessions, assuming the sign of the associations remains consistent. Thus, the sum of estimates approximates $\sum_{l=1}^m |\rho_{ij}^{(S,l)}|$, which equals zero under the null. To account for varying sample sizes across sessions, we weight the estimates by $\sqrt{n_l p}$ and define the test statistic as $\hat{T}_{ij} := \frac{1}{\sqrt{m}} \sum_{l=1}^m \sqrt{n_l p} \hat{\rho}_{ij}^{(S,l)}$. In Proposition 4.2, we show that \hat{T}_{ij} asymptotically follows a normal distribution with mean $T_{ij} := \frac{1}{\sqrt{m}} \sum_{l=1}^m \sqrt{n_l p} \rho_{ij}^{(S,l)}$, so \hat{T}_{ij} should be significantly greater than zero under the alternative hypothesis. Once the asymptotic variance is consistently estimated, constructing a confidence interval for T_{ij} and the corresponding p -value for $H_{0,ij}$ is straightforward. However, we shift our focus to the more challenging multiple edge test, treating the single edge test as a trivial special case.

Remark 3.1. More generally, additional sign information on elements of the alternative $\rho_{ij}^{(S,l)}$ may be available. With this additional knowledge, we present a test statistic based on a linear combination of those $\hat{\rho}_{ij}^{(S,l)}$ for $l = 1, \dots, m$, which is closely related to its ℓ_1 norm. More specifically, with an edge-specific sign vector $\sigma_{ij} := (\sigma_{ij}^{(1)}, \dots, \sigma_{ij}^{(m)})^\top \in \{-1, 1\}^m$, we replace \hat{T}_{ij} with the following sign-addressed test statistic $\hat{T}_{ij,\sigma} := \frac{1}{\sqrt{m}} \sum_{l=1}^m \sigma_{ij}^{(l)} \sqrt{n_l p} \hat{\rho}_{ij}^{(S,l)}$. The normal approximation we establish in Section 4 also applies to the sign-addressed test statistic.

3.2.2 Simultaneous Test

In the multiple edge test scenario, we aim to test whether there are no edges at all in a user-specified edge set E , which corresponds to the following null hypothesis:

$$H_{0,E} : \rho_{ij}^{(S,l)} = 0, \quad \forall (i, j) \in E, \quad \forall l = 1, \dots, m.$$

When E consists of a single edge (i, j) , $H_{0,E}$ reduces to the single-edge null hypothesis $H_{0,ij}$ in Eq. (5). While multiple testing techniques, such as Bonferroni correction, can be applied to extend single-edge tests to multiple-edge tests, these methods are often overly conservative. Moreover, in neuroscience applications, the edge set E typically represents connections between different brain areas, and its cardinality can grow up to q^2 . As a result, even if we establish the asymptotic normality of a single \hat{T}_{ij} , traditional multiple testing methods may not be valid in high-dimensional settings where $|E|$ grows rapidly.

To address this challenge, we propose a simultaneous testing approach based on the supremum norm of $\hat{T}_E := (\hat{T}_{ij} : (i, j) \in E)$, defined as:

$$\|\hat{T}_E\|_\infty := \max_{(i,j) \in E} |\hat{T}_{ij}|. \quad (6)$$

The key idea leverages high-dimensional central limit theory (e.g., Chernozhukov et al., 2013): although the full vector \hat{T}_E may not be asymptotically normal as $|E|$ increases, the supremum norm $\|\hat{T}_E - T_E\|_\infty$ exhibits the same limiting behavior as $\|Z\|_\infty$, where Z is a centered normal random vector with the same covariance as the asymptotic covariance of \hat{T}_E . Specifically, this covariance is given by the matrix of asymptotic covariances between $\hat{T}_{i_1 j_1}$ and $\hat{T}_{i_2 j_2}$ for $(i_1, j_1), (i_2, j_2) \in E$, expressed as:

$$S_{(i_1, j_1), (i_2, j_2)} := \sum_{l=1}^m \frac{\|\Sigma(\mathcal{T}, l)\|_F^2}{mp} \begin{bmatrix} \rho_{i_1 i_2}^{(S,l)} \rho_{j_1 j_2}^{(S,l)} + \rho_{i_1 j_2}^{(S,l)} \rho_{i_2 j_1}^{(S,l)} + \frac{1}{2} \rho_{i_1 j_1}^{(S,l)} \rho_{i_2 j_2}^{(S,l)} \left(\rho_{i_1 i_2}^{(S,l)2} + \rho_{j_1 j_2}^{(S,l)2} + \rho_{i_1 j_2}^{(S,l)2} + \rho_{i_2 j_1}^{(S,l)2} \right) \\ - \rho_{i_1 i_2}^{(S,l)} \rho_{i_2 j_2}^{(S,l)} \rho_{i_2 j_1}^{(S,l)} - \rho_{i_1 i_2}^{(S,l)} \rho_{i_1 j_1}^{(S,l)} \rho_{i_1 j_2}^{(S,l)} - \rho_{j_1 j_2}^{(S,l)} \rho_{i_2 j_2}^{(S,l)} \rho_{i_1 j_2}^{(S,l)} - \rho_{j_1 j_2}^{(S,l)} \rho_{i_2 j_1}^{(S,l)} \rho_{i_1 j_1}^{(S,l)} \end{bmatrix}. \quad (7)$$

We approximate the distribution of $\|Z\|_\infty$ using a parametric bootstrap based on the plug-in estimator \hat{S}_{EE} of the asymptotic covariance. By generating bootstrap samples from $\hat{Z} \sim N(0, \hat{S}_{EE})$, we construct a $(1 - \alpha)$ confidence

region:

$$\mathcal{C}_E(1 - \alpha) := \left\{ T_E : \|\widehat{T}_E - T_E\|_\infty = \max_{(i,j) \in E} \left| \frac{1}{\sqrt{m}} \sum_{l=1}^m \sqrt{n_l p} (\widehat{\rho}_{ij}^{(S,l)} - \rho_{ij}^{(S,l)}) \right| \leq \widehat{q}_{\|\widehat{Z}\|_\infty, 1-\alpha} \right\}, \quad (8)$$

where $\widehat{q}_{\|\widehat{Z}\|_\infty, 1-\alpha}$ is the bootstrap $(1 - \alpha)$ quantile of $\|\widehat{Z}\|_\infty$. The null hypothesis $H_{0,E}$ is rejected if $\mathbf{0} \notin \mathcal{C}_E(1 - \alpha)$. This confidence region can also be extended to c -level tests (Qiu and Zhou, 2020). The coverage of this confidence region is studied in Theorem 4.3, with a power analysis provided in Theorem 4.4. We further discuss how borrowing information across sessions enhances testing power in Remark 4.5.

3.3 Estimation of Temporal Covariance Matrix

The plug-in estimator \widehat{S}_{EE} of the asymptotic covariance (Eq. (7)) requires the Frobenius norm of the temporal covariance matrix, $\Sigma^{(\mathcal{T},l)}$ for each session. We propose to estimate $\Sigma^{(\mathcal{T},l)}$ based on a modified Cholesky decomposition of its inverse, the temporal precision matrix $\Omega^{(\mathcal{T},l)}$ (Bickel and Levina, 2008; Liu and Ren, 2020). The Cholesky decomposition reveals the natural auto-regressive relationship between the signal at a particular time point and the past signals for spatiotemporal data. Suppose that the modified Cholesky decomposition of $\Omega^{(\mathcal{T},l)}$ is $\Omega^{(\mathcal{T},l)} = L^{(\mathcal{T},l)} D^{(\mathcal{T},l)} L^{(\mathcal{T},l)\top}$, where $D^{(\mathcal{T},l)}$ is a diagonal matrix, and $L^{(\mathcal{T},l)}$ is a lower triangular matrix with diagonal entries equal to 1. Let $\beta^{(\mathcal{T},l)} := I - L^{(\mathcal{T},l)\top}$ and $\Phi^{(\mathcal{T},l)} = \frac{\text{tr}(\Sigma^{(S,l)})}{q} (D^{(\mathcal{T},l)})^{-1}$ so that the Cholesky decomposition of $\Omega^{(\mathcal{T},l)}$ can be rewritten by

$$\Omega^{(\mathcal{T},l)} = \frac{\text{tr}(\Sigma^{(S,l)})}{q} (I - \beta^{(\mathcal{T},l)})^\top (\Phi^{(\mathcal{T},l)})^{-1} (I - \beta^{(\mathcal{T},l)}). \quad (9)$$

Motivated by our working example, where temporal alignment of neural recordings is not guaranteed due to response latencies to stimuli (Ventura, 2004), we do not assume that $\Sigma^{(\mathcal{T},l)}$ is the same or even similar across sessions. Instead, we impose a weaker bandable assumption on the modified Cholesky decomposition for each session. In physiological time-series signals, the dependence between time points naturally decays as the time lag increases, so a reasonable assumption is that $\beta_{st}^{(\mathcal{T},l)}$ approaches zero as $t - s \rightarrow \infty$. By applying bandable assumptions, we ignore weak dependencies between distant time points, achieving a bias-variance trade-off in the estimation of $\beta^{(\mathcal{T},l)}$.

We estimate $\beta^{(\mathcal{T},l)}$ following the procedure in Liu and Ren (2020). Specifically, we treat the observed data $X^{(k,l)}$ at trial k and session l as q vector-variate ‘‘column samples’’ and fit the following linear regression model at each time point t :

$$\widehat{\beta}_{:,t}^{(\mathcal{T},l)} := \underset{b \in \mathbb{R}^p}{\text{argmin}} \frac{1}{2n_l q} \sum_{k=1}^{n_l} \|X_{t,\cdot}^{(k,l)} - X^{(k,l)\top} b\|_2^2 \quad (10)$$

with respect to $b_s = 0$ where $s < t - h_l$ or $s \geq t$, where the bandwidth h_l can be either user-specified or data-driven. Unlike the spatial case, the estimation of the temporal covariance matrix is performed individually for each session. Having the regression coefficients estimated, we estimate $\Phi^{(\mathcal{T},l)}$ by

$$\widehat{\Phi}_{tt}^{(\mathcal{T},l)} = \frac{1}{n_l q} \sum_{k=1}^{n_l} \|X_{t,\cdot}^{(k,l)} - X^{(k,l)\top} \widehat{\beta}_{:,t}^{(\mathcal{T},l)}\|_2^2. \quad (11)$$

For technical issues, we truncate the eigenvalues of $I - \beta^{(\mathcal{T},l)}$, following the approach in Liu and Ren (2020). For a square matrix A , let $P_\eta(A) := U \max\{\min\{\Lambda, \eta\}, \eta^{-1}\} V^\top$, where A has a singular value decomposition $A = U \Lambda V^\top$ and the min and max above are element-wise operations. Let $\overline{\Omega}^{(\mathcal{T},l)}$ be the precursor estimator of $\Omega^{(\mathcal{T},l)}$ given by

$$\overline{\Omega}^{(\mathcal{T},l)} = P_\eta(I - \widehat{\beta}^{(\mathcal{T},l)})^\top (\widehat{\Phi}^{(\mathcal{T},l)})^{-1} P_\eta(I - \widehat{\beta}^{(\mathcal{T},l)}). \quad (12)$$

In the end, due to the identifiability constraint $\text{tr}(\Sigma^{(\mathcal{T},l)}) = p$, we propose our estimators of $\Sigma^{(\mathcal{T},l)}$ and $\Omega^{(\mathcal{T},l)}$ as

$$\widehat{\Sigma}^{(\mathcal{T},l)} = \frac{p}{\text{tr}(\overline{\Sigma}^{(\mathcal{T},l)})} \overline{\Sigma}^{(\mathcal{T},l)} \quad \text{and} \quad \widehat{\Omega}^{(\mathcal{T},l)} = \frac{\text{tr}(\overline{\Sigma}^{(\mathcal{T},l)})}{p} \overline{\Omega}^{(\mathcal{T},l)}, \quad (13)$$

where $\overline{\Sigma}^{(\mathcal{T},l)} := \overline{\Omega}^{(\mathcal{T},l)-1}$.

4 Theoretical Properties

We make the following assumptions on the observed dataset.

Assumption 1. $\max_{l=1,\dots,m} \frac{n_l}{n_0} \leq \kappa_1$ for some positive constant κ_1 where $n_0 = \min_{l=1,\dots,m} n_l$.

Assumption 2. $\text{tr}(\Sigma^{(\mathcal{T},l)}) = p, \forall l = 1, \dots, m$.

Assumption 3. For $l = 1, \dots, m$, let $\{\lambda_i^{(\mathcal{T},l)}\}_{i=1,\dots,p}$ are the eigenvalues of $\Sigma^{(\mathcal{T},l)}$ while $\frac{1}{\kappa_3} \leq \lambda_1^{(\mathcal{T},l)} \leq \lambda_2^{(\mathcal{T},l)} \leq \dots \leq \lambda_p^{(\mathcal{T},l)} \leq \kappa_3$ for some constant $\kappa_3 > 0$; define and assume $\{\lambda_i^{(\mathcal{S},l)}\}_{i=1,\dots,q}$ similarly for $\Sigma^{(\mathcal{S},l)}$.

Assumption 4. Let d be the group-wise maximum node degree, i.e.,

$$d := \max_i \left| \left\{ j \in [p] \setminus \{i\} : \Omega_{ij}^{(\mathcal{S},l)} \neq 0 \text{ for some } l \in [m] \right\} \right|.$$

We assume group sparsity of the partial-correlation graph in spatial association by $d \cdot \frac{\max\{m, \log(mn_0pq)\}}{(mn_0p)^{1/2}} \rightarrow 0$ as $n_0 \rightarrow \infty$.

Assumption 5. We assume the temporal precision matrix $\Omega^{(\mathcal{T},l)}$ for each $l = 1, \dots, m$ has Cholesky decomposition as in Eq. (9) where $\beta^{(\mathcal{T},l)}$ satisfies $|\beta_{st}^{(\mathcal{T},l)}| < \kappa_5 (t-s)^{-\alpha_l-1}$ for any t and s such that $s < t$ and some $\alpha_l > 0$. We further assume that, for $\alpha_0 = \min_{l=1,\dots,m} \alpha_l$, $\frac{\log(mn_0pq)}{(n_0q)^{1-1/(\alpha_0+1)}} \rightarrow 0$ as $n_0 \rightarrow \infty$.

Assumption 1 assumes that the sample sizes across graphs are balanced, with n_0 representing this common level. Assumption 2 ensures identifiability. Assumption 3 is a standard assumption on eigenvalues commonly used in covariance estimation and graphical models (Cai et al., 2016b). Assumption 4 assumes that the spatial (column) precision matrices are sparse, and it imposes a constraint on the spatial dimension relative to the number of samples, the temporal dimension, and the number of graphs. The first part of Assumption 5 is reasonable for neural time series, as neural data, particularly LFPs, are often modeled as a low-order autoregressive process, a common assumption in the literature (Bickel and Levina, 2008; Liu and Ren, 2020). The second part, similar to Assumption 4, restricts the temporal dimension.

In the following, $C(\dots)$ indicates a constant that depends on the other constants within the parentheses, with values that may change across lines. For universal constants without any dependency, we omit the parentheses and denote them simply by C .

4.1 Non-asymptotic error bound for the group Lasso estimate

We first provide a theoretical justification for our group Lasso procedure proposed in Section 3.1. Although with correlated rows, our results below demonstrate that the optimal convergence rates for the estimation error, defined as $\Delta_{\cdot,i}^{(\mathcal{S},l)} := \widehat{\beta}_{\cdot,i}^{(\mathcal{S},l)} - \beta_{\cdot,i}^{(\mathcal{S},l)}$, and prediction can be still obtained compared to the case with i.i.d. samples. The proof is provided in Appendix B.2.

Theorem 4.1. Suppose that γ_i satisfies $\frac{1}{C(\kappa_1, \kappa_3)} \sqrt{\frac{m + \log(mn_0pq)}{n_0p}} \leq \gamma_i \leq C(\kappa_1, \kappa_3) \sqrt{\frac{m + \log(mn_0pq)}{n_0p}}$ for some sufficiently large $C(\kappa_1, \kappa_3)$. Then, under Assumptions 1 to 5,

$$\mathbb{P} \left[\begin{array}{l} \max_i \sum_{j:j \neq i} \left\| \underline{\Delta}_{ji}^{(\mathcal{S},\cdot)} \right\|_2^2 \leq C(\kappa_1, \kappa_3) d \frac{m + \log(mn_0pq)}{n_0p}, \\ \max_i \sum_{j:j \neq i} \left\| \underline{\Delta}_{ji}^{(\mathcal{S},\cdot)} \right\|_2 \leq C(\kappa_1, \kappa_3) d \sqrt{\frac{m + \log(mn_0pq)}{n_0p}}, \\ \max_i \frac{1}{2n_0p} \sum_{l=1}^m \sum_{k=1}^{n_l} \left\| X^{(k,l)} \Delta_{\cdot,i}^{(\mathcal{S},l)} \right\|_2^2 \leq C(\kappa_1, \kappa_3) d \frac{m + \log(mn_0pq)}{n_0p} \end{array} \right] \geq 1 - C(mn_0pq)^{-1/2},$$

for a sufficiently large n_0 , where $\underline{\Delta}_j^{(\mathcal{S},l)} := \frac{\|X_{\cdot,j}^{(\mathcal{S},l)}\|_2}{\sqrt{n_l p}} \Delta_j^{(\mathcal{S},l)}$.

4.2 Theoretical justification for the simultaneous edge testing

We now present the theoretical results for the simultaneous test in Section 3.2. In the proof of Proposition 4.2, we show that the error in the partial correlation estimate $\hat{\rho}_{ij}^{(S,l)}$ from Eq. (4) is dominated by the leading term

$$\Theta_{ij}^{(S,l)} := \frac{\tilde{\phi}_{ij}^{(S,l)}}{\sqrt{\Phi_{ii}^{(S,l)}\Phi_{jj}^{(S,l)}}} - \frac{\Phi_{ij}^{(S,l)}\tilde{\phi}_{jj}^{(S,l)}}{2\Phi_{jj}^{(S,l)}\sqrt{\Phi_{ii}^{(S,l)}\Phi_{jj}^{(S,l)}}} - \frac{\Phi_{ij}^{(S,l)}\tilde{\phi}_{ii}^{(S,l)}}{2\Phi_{ii}^{(S,l)}\sqrt{\Phi_{ii}^{(S,l)}\Phi_{jj}^{(S,l)}}}, \quad (14)$$

where $\tilde{\phi}_{ij}^{(S,l)} := \tilde{\Phi}_{ij}^{(S,l)} - \Phi_{ij}^{(S,l)}$ is the empirical error, given by $\tilde{\phi}_{ij}^{(S,l)} = \frac{1}{n_l p} \sum_{k=1}^{n_l} \epsilon_{\cdot,i}^{(S,k,l)\top} \epsilon_{\cdot,j}^{(S,k,l)} - \Phi_{ij}^{(S,l)}$. Since the leading error term $\Theta_{ij}^{(S,l)}$ is a linear functional of $\tilde{\phi}_{ij}^{(S,l)}$, which is an average over $t = 1, \dots, p$ and $k = 1, \dots, n_l$, the central limit theorem ensures that the partial correlation estimate $\hat{\rho}_{ij}^{(S,l)}$ and the single-edge test statistic \hat{T}_{ij} converge in distribution to Gaussian limits for each edge (i, j) .

For the multiple-edge test statistic $\|\hat{T}_E\|_\infty$, the Gaussian approximation error is related to Berry–Esseen bounds over hyper-rectangles. The seminal work of Chernozhukov et al. (2013) established such bounds under high-dimensional settings, where the dimension exceeds the sample size. Subsequent works, as reviewed by Chernozhukov et al. (2023a), have focused on improving the convergence rates. Recently, Chernozhukov et al. (2023b) achieved a near-optimal rate, which we use to derive a sharp Gaussian approximation error bound for $\|\hat{T}_E\|_\infty$. The proof is detailed in Appendix B.3.

Proposition 4.2. *Let $Z \sim N(0, S_{EE})$ where the elements of S_{EE} are given as in Eq. (7), and \hat{T}_E is estimated based on γ_i 's given as in Theorem 4.1. Then under Assumptions 1 to 5,*

$$\begin{aligned} & \sup_{x>0} \left| \mathbb{P}[\|\hat{T}_E - T_E\|_\infty > x] - \mathbb{P}[\|Z\|_\infty > x] \right| \\ & \leq \frac{C(\kappa_1, \kappa_3)}{\sqrt{mn_0p}} \max \left\{ (\log|E|)^2 \log(mn_0p), (\log|E|)^{5/2}, d\sqrt{\log|E|}(m + \log(mn_0pq)) \right\}, \end{aligned}$$

for a sufficiently large n_0 .

The following theorem mirrors the previous proposition, with the key difference being that we replace the population covariance S_{EE} with its plug-in estimator \hat{S}_{EE} . In essence, as long as S_{EE} is well-estimated under the $\|\cdot\|_\infty$ -norm, the Gaussian approximation results remain valid. Using the convergence rate of \hat{S}_{EE} in the $\|\cdot\|_\infty$ -norm, we derive the following bootstrap theorem, based on the relationship between convergence rate and bootstrap error as given in Lemma 2.1 of Chernozhukov et al. (2023b).

Theorem 4.3. *Let $\hat{Z} \sim N(0, \hat{S}_{EE})$ where the plug-in estimator \hat{S}_{EE} and \hat{T}_E are estimated based on γ_i 's given in Theorem 4.1. Then, under Assumptions 1 to 5,*

$$\begin{aligned} & \sup_{x>0} \left| \mathbb{P}[\|\hat{T}_E - T_E\|_\infty > x] - \mathbb{P}[\|\hat{Z}\|_\infty > x | \mathcal{D}] \right| \\ & \leq C(\kappa_1, \kappa_3, \kappa_5) \max \left\{ \frac{(\log|E|)^2 \log(mn_0p)}{\sqrt{mn_0p}}, \frac{(\log|E|)^{5/2}}{\sqrt{mn_0p}}, d\sqrt{\log|E|} \frac{m + \log(mn_0pq)}{\sqrt{mn_0p}}, \right. \\ & \quad \left. \log|E| \log(n_0pq) \sqrt{\frac{\log(mn_0pq)}{(n_0q)^{1 - \frac{1}{2(\alpha_0+1)}}} + \frac{m + \log(mn_0pq)}{mn_0p}} \right\} \end{aligned}$$

with probability at least $1 - C(mn_0pq)^{-1/2}$ for a sufficiently large n_0 .

The above theorem establishes the theoretical foundation for the simultaneous multiple edge testing procedure in Algorithm 1. Next, we formally state the validity of our testing procedure as well as a power analysis. The proof is given in Appendix B.5.

Theorem 4.4. *Suppose that n_0 increases at a faster rate than*

$$\frac{1}{mp} \max \left\{ (\log|E|)^4 (\log(mn_0p))^2, (\log|E|)^5, d^2 \log|E| (m + \log(mn_0pq))^2, (\log|E| \log(n_0p))^2 (m + \log(mn_0pq)) \right\}$$

and $\frac{1}{q} ((\log|E| \log(n_0q))^2 \log(mn_0pq))^{1+1/(2\alpha_0+1)}$. Under the null $H_{0,E}$ and Assumptions 1 to 5, the confidence region $\mathcal{C}_E(1 - \alpha)$ estimated based on γ_i 's given in Theorem 4.1 satisfies $\mathbb{P}[\mathbf{0} \notin \mathcal{C}_E(1 - \alpha)] \xrightarrow{p} \alpha$. On the other hand,

as an alternative, if

$$\|T_E\|_\infty \geq C(\kappa_1, \kappa_3, \kappa_5) \sqrt{(\log q + \log(1/\alpha)) \max_{(i,j) \in E} S_{(i,j),(i,j)}},$$

then under the same assumptions and γ_i 's, we have $\mathbb{P}[\mathbf{0} \notin \mathcal{C}_E(1 - \alpha)] \xrightarrow{p} 1$.

Remark 4.5. The theorem implies that as long as the sum of the partial correlations $\rho_{ij}^{(S,l)}$ across l , i.e., $\sum_{l=1}^m |\rho_{ij}^{(S,l)}|$, is above the order of $\sqrt{m \log q / (n_0 p)}$ for some $(i, j) \in E$, the power converges to 1 as $n_0 \rightarrow \infty$. Assuming the same order of $\rho_{ij}^{(S,l)}$ across sessions, the power of the test converges to 1 as $n_0 \rightarrow \infty$, if $\max_{(i,j) \in E} |\rho_{ij}^{(S,l)}|$ is larger than $\sqrt{\log q / (mn_0 p)}$. In contrast, the corresponding detection boundary is $\sqrt{\log q / (n_0 p)}$ if we do not aggregate multiple graphs. Therefore, by borrowing the information from multiple graphs or sessions, we can reduce the detection accuracy by a factor of root m . In addition, when the temporal covariance matrix $\Sigma^{(\mathcal{T},l)} = I$ for all $l = 1, \dots, m$, the model reduces to the multiple vector-variate Gaussian graphical model, as studied in Ren et al. (2019), with an effective sample size $n_0 p$. According to their Theorem 2.3, the optimal separating rate for detecting a single edge, in terms of the sum of the partial correlations, is $\sqrt{m / (n_0 p)}$. This suggests that our linear functional-based test is nearly optimal in achieving the testable region boundary.

4.3 Non-asymptotic error bound for the temporal covariance matrix estimate

In this section, we present the estimation error bounds for the session-specific temporal covariance and precision matrices obtained in Section 3.3. While results for i.i.d. samples are available in Liu and Ren (2020), no such results exist for the correlated samples considered in our model. Therefore, we provide a self-contained analysis, which may be of independent interest. The proof is detailed in Appendix B.7.

Proposition 4.6. Suppose that $h_l = \lfloor (n_l q)^{1/(1+\alpha_0)} \rfloor$. Then, following the procedure defined in Section 3.3,

$$\mathbb{P} \left[\max_l \max_{1 \leq t \leq p} \|\widehat{\beta}_{\cdot,t}^{(\mathcal{T},l)} - \beta_{\cdot,t}^{(\mathcal{T},l)}\|_2 \geq C(\kappa_1, \kappa_3, \kappa_5) \sqrt{\frac{\log(mn_0 pq)}{(n_0 q)^{1-1/(2\alpha_0+2)}}} \right] \leq C(mn_0 pq)^{-1/2},$$

$$\mathbb{P} \left[\max_l \max_{1 \leq t \leq p} \left| \widehat{\Phi}_{tt}^{(\mathcal{T},l)} - \frac{\text{tr}(\Sigma^{(S,l)})}{q} \Phi_{tt}^{(\mathcal{T},l)} \right| \geq C(\kappa_1, \kappa_3, \kappa_5) \sqrt{\frac{\log(mn_0 pq)}{(n_0 q)^{1-1/(2\alpha_0+2)}}} \right] \leq C(mn_0 pq)^{-1/2}.$$

Theorem 4.7. Suppose that $h_l = \lfloor (n_l q)^{1/(1+\alpha_0)} \rfloor$ and $\eta = C(\kappa_3)$ satisfies $\eta \leq \lambda_1(I - \beta^{(\mathcal{T},l)})$ for $l = 1, \dots, m$, where $\lambda_1(I - \beta^{(\mathcal{T},l)})$ is the smallest eigenvalue of $I - \beta^{(\mathcal{T},l)}$. Then,

$$\mathbb{P} \left[\begin{array}{l} \max_l \frac{1}{p} \left\| \widehat{\Sigma}^{(\mathcal{T},l)} - \frac{\text{tr}(\Sigma^{(S,l)})}{q} \Sigma^{(\mathcal{T},l)} \right\|_F^2 \geq C(\kappa_1, \kappa_3, \kappa_5) \frac{\log(mn_0 pq)}{(n_0 q)^{1-1/(2\alpha_0+2)}}, \\ \max_l \frac{1}{p} \left\| \widehat{\Omega}^{(\mathcal{T},l)} - \frac{q}{\text{tr}(\Sigma^{(S,l)})} \Omega^{(\mathcal{T},l)} \right\|_F^2 \geq C(\kappa_1, \kappa_3, \kappa_5) \frac{\log(mn_0 pq)}{(n_0 q)^{1-1/(2\alpha_0+2)}} \end{array} \right] \leq C(mn_0 pq)^{-1/2}.$$

Consequently, the Frobenius norms of $\Sigma^{(\mathcal{T},l)}$ can be consistently estimated, which is sufficient for our main result Theorem 4.3. The proof is given in Appendix B.8.

Corollary 4.8. Suppose that $h_l = \lfloor (n_l q)^{1/(1+\alpha_0)} \rfloor$ and $\eta = C(\kappa_3)$ satisfies $\eta \leq \lambda_1(I - \beta^{(\mathcal{T},l)})$ for $l = 1, \dots, m$. Then,

$$\mathbb{P} \left[\max_l \left| \frac{\|\widehat{\Sigma}^{(\mathcal{T},l)}\|_F^2 - \|\Sigma^{(\mathcal{T},l)}\|_F^2}{p} \right| \geq C(\kappa_1, \kappa_3, \kappa_5) \frac{\log(mn_0 pq)}{(n_0 q)^{1-1/(2\alpha_0+2)}} \right] \leq C(mn_0 pq)^{-1/2}$$

for sufficiently large n_0 .

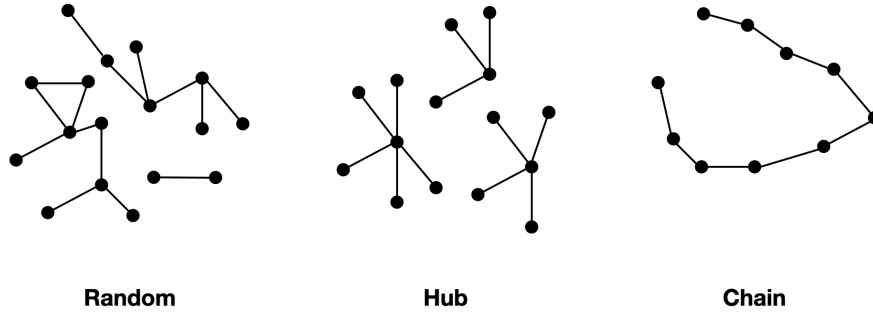


Figure 1: Simulated spatial graphs.

5 Numerical Studies

In Section 5.1, we present simulation studies to validate our theoretical results of Section 4 and evaluate the performance of our matrix-variate graphical models in comparison to several baseline approaches. In Section 5.2, we apply our method to neural recordings from two Utah arrays implanted in monkey brains during a spatial working memory task. The implementation of our proposed method is available in the `mmge` R package, along with vignettes for reproducing our results, accessible at github.com/HeejongBong/mmge.

5.1 Simulation Studies

We evaluated the performance of our method under three spatial graph structures, illustrated in Figure 1: (1) a random graph, where edges between nodes were generated with probability $\sqrt{\frac{3}{q}}$ for each pair (i, j) ; (2) a hub graph, where the nodes were divided into $\lceil \frac{q}{20} \rceil$ hub groups; and (3) a chain graph. Given each spatial graph structure, we generated the spatial precision matrix by sampling the non-zero entries from $\text{Unif}(0, \frac{0.3}{2^{i-1}})$, independently across sessions $l = 1, \dots, m$. For the temporal precision matrix, we generated $\Sigma^{(\mathcal{T}, l)}$ using Eq. (9). Following Assumption 5, we set $\beta_{st}^{(\mathcal{T}, l)} = \kappa_5 (t - s)^{-\alpha_l - 1}$ for $1 \leq s < t \leq p$, with $\kappa_5 = 0.2$ and $\alpha_l = 1$. For $\Phi^{(\mathcal{T}, l)}$, we used the $p \times p$ identity matrix for all $l = 1, \dots, m$.

In Section 5.1.1, we compare our method’s performance with existing methods in terms of edge detection and precision matrix estimation. In Section 5.1.2, we assess the coverage of the proposed bootstrap confidence region for $\|T_E\|_\infty$.

5.1.1 Edge-wise Estimation Comparison

We compared our method (M0) with the following Gaussian graphical model estimation procedures:

- (M1): matrix-variate Gaussian multi-graph estimation method by Zhu and Li (2018)
- (M2): regression-based Gaussian graphical model estimation method by Ren et al. (2019)
- (M3 & M4): optimization based Gaussian graphical model estimation methods Cai et al. (2016a) and Lee and Liu (2015), respectively

Methods (M0) and (M1) are based on the matrix-variate Gaussian model, while the others are designed for the vector-variate model. Since the vector-variate model does not account for temporal correlation, methods (M2), (M3), and (M4) are at a disadvantage when applied to matrix-variate data. To ensure a fair comparison, we used the `whiten` function from the `whitening` R package to whiten the simulated data before applying the vector-variate methods.

The edge detection performance of the methods was evaluated using receiver operating characteristic (ROC) curves. An ROC curve plots the true positive rate (TPR) against the false positive rate (FPR) as the detection threshold is varied by adjusting specific hyperparameters. For Methods (M0) and (M2), which detect non-zero spatial edges based on rejecting edge-wise null hypotheses (Eq. (5)), we generated ROC curves by varying the p -value threshold while keeping other hyperparameters fixed. For the sparsity hyperparameter of Method (M0), we fixed $\gamma_i = 1e - 4$ for all i . For the remaining methods, ROC curves were plotted by adjusting the sparsity-controlling hyperparameter, with all other hyperparameters held constant.

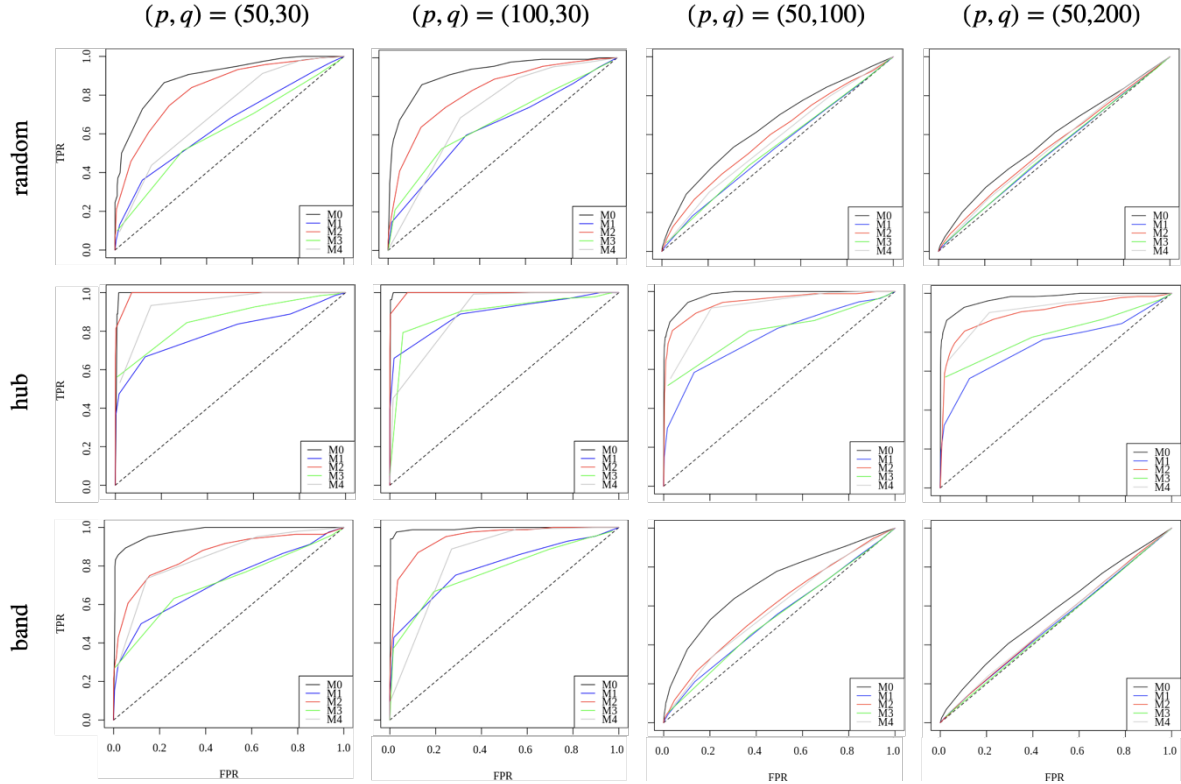


Figure 2: Simulation results are shown for different graph configurations and temporal dimensions with $n = 5$ and $m = 5$. Rows represent different graph types, while columns correspond to varying spatial and temporal dimensions. The black curves represent our method (M0), with other colors representing baseline methods.

The results with $m = 5$, $n = 5$, and four different pairs of (p, q) are shown in Fig. 2. The ROC curves indicate that our method consistently outperformed the other methods, thanks to the efficient use of spatial observations across sessions. In an additional simulation study with varying γ_i values, our method demonstrated moderate sensitivity to the choice of the group lasso hyperparameter, while it consistently outperformed the baseline methods across the range of tuning parameters considered, particularly in settings with high temporal and spatial dimensions.

5.1.2 Simultaneous Test

In this section, we evaluate the coverage of the proposed bootstrap confidence interval (Eq. (8)) using simulated data. The simulations were conducted with m sessions of n i.i.d. matrix-variate data, with temporal dimension $p = 50$ and spatial dimension $q = 30$. We generated 3000 bootstrap samples to construct confidence intervals for $\|T_E\|_\infty$ over two edge sets: $E_{\text{off}} = \{(i, j) : i \neq j\}$ and $E_{\text{zero}} = \{(i, j) : \Omega_{ij}^{(S,l)} = 0, \forall l = 1, \dots, m\}$.

We repeated this procedure over 1000 datasets generated from the multiple matrix-variate Gaussian graphical models for each of the three spatial partial-correlation graphs (random, hub, and chain). For each graph, we computed the empirical coverage of the bootstrap confidence intervals. Table 1 presents the mean and standard deviation of the empirical coverage across the 1000 repetitions for each spatial graph and nominal coverage level. We observe that the empirical coverages are close to the nominal values and converge further as the sample size n increases. This result demonstrates the coverage of the bootstrap confidence region shown in Theorem 4.3.

5.2 Experimental Data Analysis

We analyzed local field potential recordings (LFPs) from two Utah arrays implanted in the prefrontal cortex (PFC) and visual area V4 of a Macaque monkey (Fig. 3(a)). Each Utah array had 96 electrodes, and the neuroelectrical activity in the two areas were simultaneously recorded during a memory-guided saccade task. One trial of the task consisted of the following stages (see Fig. 3(b)):

Table 1: Empirical coverage of the confidence region for $m = 5, p = 50, q = 30$.

n	nominal coverage	Random		Hub		Chain	
		E_{off}	E_{zero}	E_{off}	E_{zero}	E_{off}	E_{zero}
5	0.925	0.906(0.009)	0.900(0.009)	0.901(0.006)	0.904(0.006)	0.886(0.008)	0.888(0.007)
	0.95	0.935(0.006)	0.938(0.006)	0.932(0.006)	0.934(0.007)	0.922(0.007)	0.923(0.008)
	0.975	0.971(0.004)	0.962(0.005)	0.962(0.004)	0.963(0.004)	0.959(0.005)	0.959(0.005)
10	0.925	0.908(0.006)	0.913(0.005)	0.931(0.005)	0.928(0.006)	0.931(0.006)	0.928(0.007)
	0.95	0.934(0.004)	0.937(0.004)	0.951(0.003)	0.950(0.003)	0.953(0.004)	0.953(0.005)
	0.975	0.961(0.004)	0.961(0.003)	0.971(0.003)	0.971(0.003)	0.974(0.003)	0.975(0.003)
20	0.925	0.917(0.007)	0.920(0.004)	0.934(0.004)	0.930(0.006)	0.931(0.006)	0.928(0.007)
	0.95	0.947(0.006)	0.948(0.005)	0.959(0.004)	0.955(0.004)	0.953(0.004)	0.953(0.005)
	0.975	0.978(0.002)	0.975(0.004)	0.985(0.002)	0.984(0.002)	0.974(0.003)	0.975(0.002)

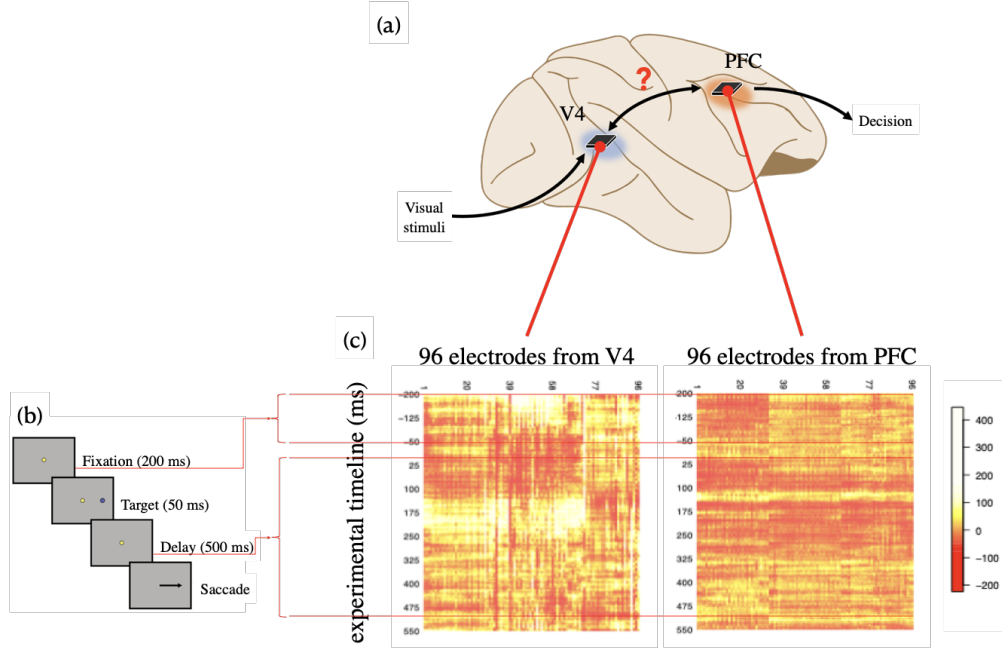


Figure 3: (a) The positions of analyzed cortical areas, V4 and PFC in a primate brain. Area PFC has been associated with top-down control of attention while area V4 is a mid-level visual area with robust visual responses. The neuroelectrical activity in each area was recorded by a 96-electrode Utah array. (b) The timeline of one experimental trial (Khanna et al., 2020). We are interested in the fixation, target presentation and delay stages of 750 ms in total. (c) LFP recordings for one experimental trial. Each x-axis indicates 96 electrodes in each brain area, and the y-axis is time in ms. Time $t = 0$ was aligned at the start of the delay period.

1. The monkey fixated at the center of the screen for 200 ms.
2. A circular target appeared at a randomly chosen location out of the forty possible spots on the screen (8 directions and 5 amplitudes) and turned off after 50 ms.
3. The monkey had to remember the target location during a delay period of 500 ms while maintaining fixation.
4. After the delay period, the fixation point turned off, and the monkey had to make a saccade to the remembered target location.

See Khanna et al. (2020) for the details of the experiment and data collection. In previous work in similar tasks, V4 has been reported to retain higher order information (e.g., color and shape) and attention to visual objects (Orban, 2008; Fries et al., 2001), while prefrontal cortex (PFC) is considered to exert cognitive control in working memory (Miller and Cohen, 2001). Despite their spatial distance and functional differentiation, these regions have been presumed to cooperate during visual memory retention (Sarnthein et al., 1998; Liebe et al., 2012).

The analyzed dataset was collected over $m = 5$ experimental sessions, which consisted of $n_l = 2000, 2995, 3000, 3000$ and 3000 successful trials. For each trial, we observed matrix-variate data of temporal dimension $p = 750$ (750 ms at sampling rate 1 kHz) and spatial dimension $q = 192$ (2×96 electrodes) in total. The data of one example trial is

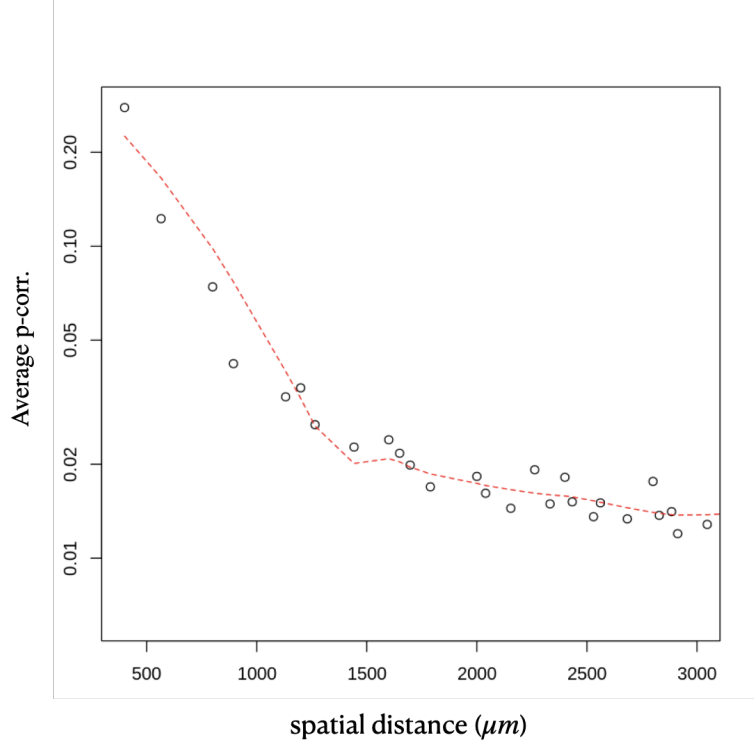


Figure 4: The averaged $\hat{\rho}_{ij}^{(S)}$ within a group of spatially equidistant within-area edges during the late delay stage in V4. Notice that the spatial partial correlation declined as the spatial distance increased. This phenomenon is consistently identified over all experimental stages and both brain areas.

shown in Fig. 3(c). The color in the heatmap corresponds to the intensity of the LFP signal. The data are available in a KiltHub repository of Carnegie Mellon University, located at <http://10.1184/R1/19248827.v1>.

Our objective is to detect changes in the spatial correlation structure within and between the brain regions across four experimental stages: fixation (200 ms), target presentation (50 ms), early delay (the first 250 ms during delay), and late delay (the last 250 ms during delay). We applied the proposed method in Section 3 separately to each stage.

5.2.1 Correlated neural connectivity vs. Physical distance

First, we applied our method separately to each brain area. We set γ_i to be the same value γ and used the cross-validation method to determine the group Lasso tuning parameter γ . Using the spatial location of the electrodes, we inferred the relationship between neural connectivity and physical distance. We looked into the average of the spatial partial correlation estimates $\hat{\rho}_{ij}^{(S)} = \frac{1}{\sum_{l=1}^m \sqrt{n_{il}p}} \sum_{l=1}^m \sqrt{n_{il}p} \hat{\rho}_{ij}^{(S,l)}$ on groups of spatially equidistant edges on the electrode array. Fig. 4 demonstrates the monotonic decreasing relationship of the averaged $\hat{\rho}_{ij}^{(S)}$ with the spatial distance at the late delay stage in V4. The same trends were observed for the other experimental stages and in PFC, advocating the previous discoveries about the strong dependency of correlated neural activity on the physical distance (Goris et al., 2014; Vinci et al., 2018). This result provides a sanity check for our spatial partial correlation estimates.

5.2.2 Within-area Inference

Next, for each electrode i , we evaluated its overall connectivity within the same region by $\sum_j |\hat{\rho}_{ij}^{(S)}|$. Fig. 5 shows the smoothed distributions of within-area connectivity for the four experimental stages and in the two brain areas. We first observed that V4 exhibited more within-area connectivity than PFC. In V4, the within-area connectivity was strongest during the fixation and cue stages and declined during the delay stages. On the other hand, the level of connectivity in PFC remained stable over the experimental stages.

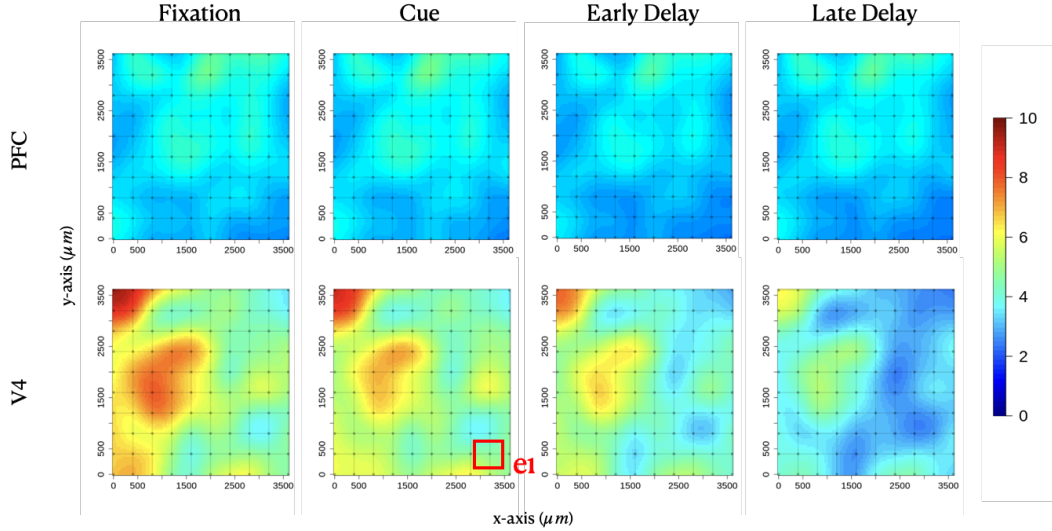


Figure 5: Spatially smoothed within-area connectivity strength distribution over the spatial electrode array for PFC and V4 over the experimental stages. The connectivity within V4 decayed over the stages, while the level of within-connectivity in PFC was stable.

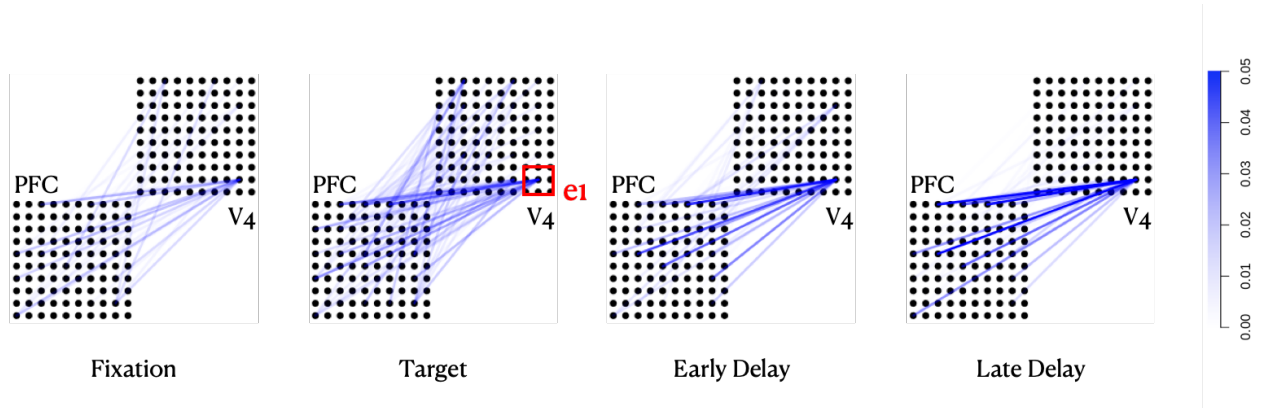


Figure 6: Estimated cross-area connectivity between PFC and V4, shown as edges color-coded by $\hat{\rho}_{ij}^{(S)}$ over the four experimental stages. The x- and y-axes are spatial coordinates of the electrodes on each array. The plot shows a spatial distinction in the evolution of the cross-area connection.

5.2.3 Cross-area Inference

Last, we applied our method to the recordings from both areas and identified significant cross-area connectivity. To reduce computation time and collinearity, we subsampled the electrodes in each area by taking every other node along the spatial dimension, reducing the spatial dimension q from 192 to 50 in total. This reduced the number of cross-area edges to 625. Also, because beta oscillations are often associated with communication across the two brain areas (Klein et al., 2020; Miller et al., 2018), we first band-pass filtered the LFP recordings at the beta band 15 – 30 Hz and downsampled the filtered data to 200 Hz. Fig. 6 shows the cross-area edges, color-coded by the estimated spatial partial correlations $\hat{\rho}_{ij}^{(S)}$. We found that the cross-area connectivity between V4 and PFC was much stronger between some electrode pairs than others, and changed substantially over time. In particular, the edges with electrode e_1 (shown red in Fig. 6) strengthened over time, whereas the other edges were strongest during the target presentation. This is broadly consistent with the finding that there are interactions between V4 and PFC during attention tasks (Squire et al., 2013; Snyder et al., 2021) and that corticocortical connections at a distance are quite sparse and highly variable in strength depending on distance and response properties (Ts'o et al., 1986; El-Shamayleh et al., 2013; Smith and Kohn, 2008).

Table 2: The c -level test results for $\|\widehat{\rho}_{E_2}\|_\infty$ at c -levels $\{0, 0.02, 0.03, 0.04\}$. Entries with * represent the significance at $\alpha = 0.05$.

c -level	Fixation	Cue	Early Delay	Late Delay
0	*	*	*	*
0.02		*	*	*
0.03			*	*
0.04				*

We analyzed cross-area connectivity in the two spatially-distinct edge sets using $\|\widehat{\rho}_{E_1}\|_\infty$ and $\|\widehat{\rho}_{E_2}\|_\infty$, where E_1 is the cross-area edges without electrode e_1 , and E_2 consists of the other edges. Fig. 7 shows the change of cross-area connectivity in the two edge sets over the four experimental stages. In E_1 , we identified that the cross-area connectivity was strongest during the target presentation. This might relate to the communication between V4 and PFC about the target stimulus. On the other hand, E_2 showed enhanced connectivity during the delay stage, when the animal had to process the visual signal and prepare the subsequent decision. The monotonicity of the cross-area connectivity in edge set E_2 was tested by the linear trend test. In the test, we linear-regressed the level of connectivity at the four stages against the respective time points on the experimental timeline. If the slope of the regression function was positive, the connectivity was increasing across the stages; if negative, the connectivity was decreasing. The p-value was estimated using 100,000 bootstrap samples. We note that this linear trend test assumed the statistics $\|\widehat{\rho}_{E_2}\|_\infty$ were independent across the stages, which might not be true. The test showed that the connectivity levels in E_2 were significantly increasing. A similar pattern was found in the averaged partial correlation in E_2 (Fig. A.1). This finding makes a remarkable contrast with the suppressed within-area connectivity in V4 during the delay stages, visible in Fig. 5. When we applied the same test to the averaged partial correlations within V4, the within-area connectivity in V4 was found to be significantly decreasing (Fig. A.2).

The cross-area connectivity trend was further evidenced by the c -level testing. By testing if $\|\rho_{E_2}\|_\infty$ exceeds threshold level c , i.e.,

$$H_{0,c} : \|\rho_{E_2}\|_\infty \leq c$$

we compared the cross-area connectivity strengths in the four stages. Table 2 shows the test results at four levels $c = 0, 0.02, 0.03, 0.04$. At $c = 0$, the cross-area connectivity in E_1 was significant with $\alpha = 0.05$ at all experimental stages. As the level increased, the tests at the early stages began unrejected. At $c = 0.04$, the test was significant only at the late delay stage. These results are consistent with our finding in Fig. 7 and the subsequent linear trend test.

Our inference results support the previous studies that neural variability in the spiking of neurons declines during the stimulus onset (Churchland et al., 2010), and visual stimuli cause a substantial decrease in the correlation of cortical neurons (Smith and Kohn, 2008). We also discovered robust sustained within-area connectivity in PFC during the delay stage, compared to V4, which was also reported by Leavitt et al. (2017).

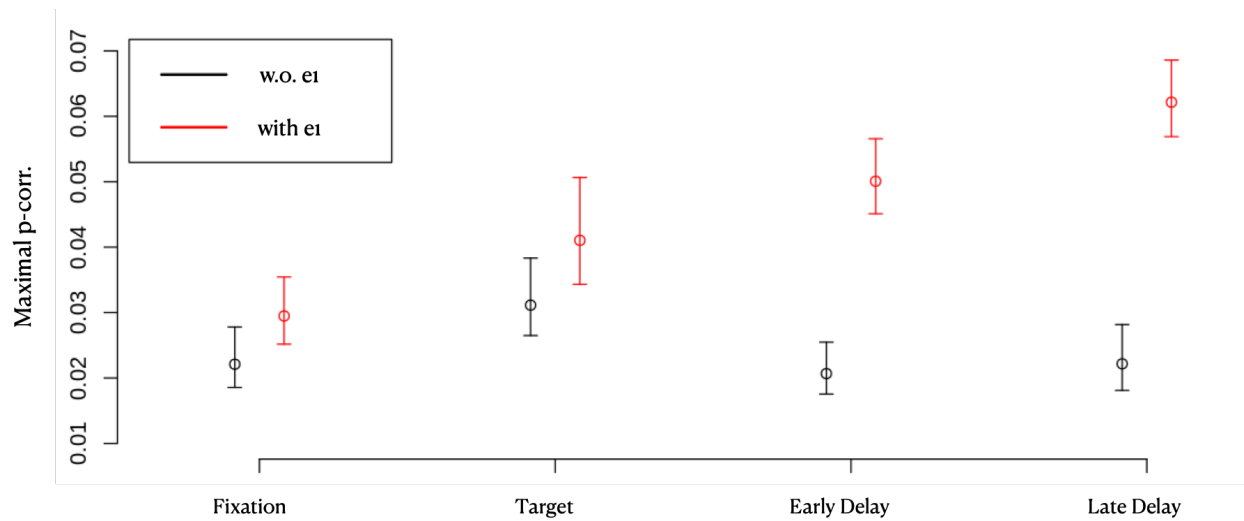


Figure 7: Inference on the maximal partial correlations over the two edge sets: (red) the cross-area edges with electrode e_1 , marked in Fig. 6 and (black) the other cross-area edges. The points are the median values of the bootstrap samples obtained by Algorithm 1 with 100,000 bootstrap samples, and the error bars are the 95% bootstrap confidence intervals. The mean spatial partial correlation over the edges with electrode e_1 was shown to be significantly monotonic increasing by the linear trend test ($p < 1e-6$).

6 Conclusion

In this paper, we propose a linear functional-based test using partial correlation estimators to detect sparse edges and to infer the existence and strength of connectivity between two groups of nodes in multiple matrix-variate Gaussian graphical models. Our approach allows the spatial and temporal dimensions, as well as the number of graphs, to diverge and potentially exceed the sample size.

Both our model and our assumptions are motivated by practical concerns in neural data analysis. In real data, we observe that the within-area connectivity and cross-area connectivity change as the animal progresses through different experimental stages. Specifically, within-area connectivity peaks during the early experimental stages, while cross-area connectivity grows when the animal processes visual signals in the late delay stage. Our inference results provide valuable insights for scientists seeking to understand the activity and connectivity of the PFC and V4 regions during visual tasks.

Our method represents the first attempt to address the simultaneous testing problem in multiple matrix-variate Gaussian graphs. An interesting future direction would be to extend this approach to other commonly used non-Gaussian graph types, such as Poisson networks. Additionally, our current implementation uses group Lasso for the regression model, which requires one tuning parameter. In the future, a tuning-free or scale-free approach, such as the self-tuned Dantzig selector or scaled Lasso, would be desirable to address issues of heterogeneity and correlation in regression with data from multiple matrix-variate Gaussian graphical models. These extensions, while beyond the scope of this work, offer promising directions for future research.

References

- Bickel, P. J. and Levina, E. (2008). Regularized estimation of large covariance matrices. *The Annals of Statistics*, 36(1):199–227.
- Buzsáki, G., Anastassiou, C. A., and Koch, C. (2012). The origin of extracellular fields and currents—eeg, ecog, lfp and spikes. *Nature reviews neuroscience*, 13(6):407–420.
- Cai, T. T., Li, H., Liu, W., and Xie, J. (2016a). Joint Estimation of Multiple High-dimensional Precision Matrices. *Statistica Sinica*, 26(2):445–464.
- Cai, T. T., Ren, Z., and Zhou, H. H. (2016b). Estimating structured high-dimensional covariance and precision matrices: Optimal rates and adaptive estimation. *Electronic Journal of Statistics*, 10(1):1–59.
- Chen, X. and Liu, W. (2018). Graph Estimation for Matrix-variate Gaussian Data. *Statistica Sinica*, 29:479–504.
- Chernozhukov, V., Chetverikov, D., and Kato, K. (2013). Gaussian approximations and multiplier bootstrap for maxima of sums of high-dimensional random vectors. *The Annals of Statistics*, 41(6):2786–2819.
- Chernozhukov, V., Chetverikov, D., Kato, K., and Koike, Y. (2023a). High-dimensional data bootstrap. *Annual Review of Statistics and Its Application*, 10:427–449.
- Chernozhukov, V., Chetverikov, D., and Koike, Y. (2023b). Nearly optimal central limit theorem and bootstrap approximations in high dimensions. *The Annals of Applied Probability*, 33(3):2374–2425.
- Churchland, M. M., Yu, B. M., Cunningham, J. P., Sugrue, L. P., Cohen, M. R., Corrado, G. S., Newsome, W. T., Clark, A. M., Hosseini, P., Scott, B. B., Bradley, D. C., Smith, M. A., Kohn, A., Movshon, J. A., Armstrong, K. M., Moore, T., Chang, S. W., Snyder, L. H., Lisberger, S. G., Priebe, N. J., Finn, I. M., Ferster, D., Ryu, S. I., Santhanam, G., Sahani, M., and Shenoy, K. V. (2010). Stimulus onset quenches neural variability: a widespread cortical phenomenon. *Nature Neuroscience*, 13(3):369–378.
- Dawid, A. P. (1981). Some matrix-variate distribution theory: notational considerations and a bayesian application. *Biometrika*, 68(1):265–274.
- El-Shamayleh, Y., Kumbhani, R. D., Dhruv, N. T., and Movshon, J. A. (2013). Visual response properties of V1 neurons projecting to V2 in macaque. *Journal of Neuroscience*, 33(42):16594–16605.
- Fornito, A., Zalesky, A., and Breakspear, M. (2013). Graph analysis of the human connectome: promise, progress, and pitfalls. *Neuroimage*, 80:426–444.
- Fries, P., Reynolds, J. H., Rorie, A. E., and Desimone, R. (2001). Modulation of oscillatory neuronal synchronization by selective visual attention. *Science*, 291(5508):1560–1563.
- Goris, R. L. T., Movshon, J. A., and Simoncelli, E. P. (2014). Partitioning neuronal variability. *Nature Neuroscience*, 17(6):858–865.
- Gubner, J. A. (2006). *Probability and random processes for electrical and computer engineers*. Cambridge University Press.
- Jones, K. E., Campbell, P. K., and Normann, R. A. (1992). A glass/silicon composite intracortical electrode array. *Annals of Biomedical Engineering*, 20(4):423–437.
- Khanna, S. B., Scott, J. A., and Smith, M. A. (2020). Dynamic shifts of visual and saccadic signals in prefrontal cortical regions 8ar and fef. *Journal of Neurophysiology*, 124(6):1774–1791.
- Klein, N., Orellana, J., Brincat, S. L., Miller, E. K., Kass, R. E., et al. (2020). Torus graphs for multivariate phase coupling analysis. *The Annals of Applied Statistics*, 14(2):635–660.
- Leavitt, M. L., Mendoza-Halliday, D., and Martinez-Trujillo, J. C. (2017). Sustained activity encoding working memories: Not fully distributed. *Trends in Neurosciences*, 40(6):328 – 346.
- Lee, W. and Liu, Y. (2015). Joint Estimation of Multiple Precision Matrices with Common Structures. *Journal of Machine Learning Research*, 16:1035–1062.
- Liebe, S., Hoerzer, G. M., Logothetis, N. K., and Rainer, G. (2012). Theta coupling between V4 and prefrontal cortex predicts visual short-term memory performance. *Nature Neuroscience*, 15:456.
- Liu, W. (2013). Gaussian graphical model estimation with false discovery rate control. *The Annals of Statistics*, 41(6):2948–2978.
- Liu, Y. and Ren, Z. (2020). Minimax estimation of large precision matrices with bandable cholesky factor. *The Annals of Statistics*, 48(4):2428–2454.
- Meinshausen, N. and Bühlmann, P. (2006). High-dimensional graphs and variable selection with the lasso. *The Annals of Statistics*, 34(3):1436–1462.

- Miller, E. K. and Cohen, J. D. (2001). An integrative theory of prefrontal cortex function. *Annual Review of Neuroscience*, 24:167–202.
- Miller, E. K., Lundqvist, M., and Bastos, A. M. (2018). Working memory 2.0. *Neuron*, 100(2):463–475.
- Orban, G. A. (2008). Higher order visual processing in macaque extrastriate cortex. *Physiological Reviews*, 88(1):59–89.
- Qiu, Y. and Zhou, X.-H. (2020). Estimating c -level partial correlation graphs with application to brain imaging. *Biostatistics*, 21(4):641–658.
- Ren, Z., Kang, Y., Fan, Y., and Lv, J. (2019). Tuning-free heterogeneous inference in massive networks. *Journal of the American Statistical Association*, 114(528):1908–1925.
- Sarnthein, J., Petsche, H., Rappelsberger, P., Shaw, G., and Von Stein, A. (1998). Synchronization between prefrontal and posterior association cortex during human working memory. *Proceedings of the National Academy of Sciences*, 95:7092–7096.
- Smith, M. A. and Kohn, A. (2008). Spatial and temporal scales of neuronal correlation in primary visual cortex. *Journal of Neuroscience*, 28(48):12591–12603.
- Snyder, A. C., Yu, B. M., and Smith, M. A. (2021). A stable population code for attention in prefrontal cortex leads a dynamic attention code in visual cortex. *Journal of Neuroscience*, 41(44):9163–9176.
- Squire, R. F., Noudoost, B., Schafer, R. J., and Moore, T. (2013). Prefrontal contributions to visual selective attention. *Annual Review of Neuroscience*, 36:451–466.
- Ts’o, D. Y., Gilbert, C. D., and Wiesel, T. N. (1986). Relationships between horizontal interactions and functional architecture in cat striate cortex as revealed by cross-correlation analysis. *Journal of Neuroscience*, 6(4):1160–1170.
- Ventura, V. (2004). Testing for and estimating latency effects for poisson and non-poisson spike trains. *Neural Computation*, 16(11):2323–2349.
- Vinci, G., Ventura, V., Smith, M. A., and Kass, R. E. (2018). Adjusted regularization of cortical covariance. *Journal of Computational Neuroscience*, 45(2):83–101.
- Yuan, M. and Lin, Y. (2006). Model selection and estimation in regression with grouped variables. *Journal of the Royal Statistical Society Series B: Statistical Methodology*, 68(1):49–67.
- Zhu, Y. and Li, L. (2018). Multiple matrix gaussian graphs estimation. *Journal of the Royal Statistical Society Series B: Statistical Methodology*, 80(5):927–950.